Strong metal–support interaction of Ru on TiO_2 derived from the co-reduction mechanism of $Ru_xTi_{1-x}O_2$ interphase

Yaru Zhang
Dalian Institute of Chemical Physics
Haifeng Qi
Dalian Institute of Chemical Physics
Xiong Su
Dalian Institute of Chemical Physics https://orcid.org/0000-0003-2232-0403
Yang Su
Dalian Institute of Chemical Physics, Chinese Academy of Sciences
Xiao Yan Liu
Chinese Academy of Sciences https://orcid.org/0000-0003-2694-2306
Lin Li
Dalian Institute of Chemical Physics
Xiaofeng Yang
Dalian Institute of Chemical Physics https://orcid.org/0000-0001-5012-5651
Yanqiang Huang (yqhuang@dicp.ac.cn)
CAS Key Laboratory of Science and Technology on Applied Catalysis, Dalian Institute of Chemical Physics, Chinese Academy of Sciences https://orcid.org/0000-0002-7556-317X
Tao Zhang
Dalian Institute of Chemical Physics, Chinese Academy of Sciences https://orcid.org/0000-0001-9470-7215

Article

Keywords: Strong metal–support interaction (SMSI), formation mechanism, Ru/TiO2, CO2 methanation

Posted Date: April 28th, 2021

DOI: https://doi.org/10.21203/rs.3.rs-448852/v1

Version of Record: A version of this preprint was published at ACS Catalysis on January 14th, 2022. See the published version at https://doi.org/10.1021/acscatal.1c04785.

Abstract

Strong metal–support interaction (SMSI) plays a crucial role in determining the catalytic performances of supported metal catalysts, in which the subsequent migration of supports over the pre-existing metal nanoparticles is generally considered during the pretreatment condition. Herein, a distinct mechanism of SMSI generation by the co-reduction of oxide interphase is addressed over the Ru/TiO_2 catalysts. Our results demonstrate that the formation of $Ru_xTi_{1-x}O_2$ oxide interphase can be facilely augmented by increasing the calcination temperature over Ru/TiO_2 catalysts, while a growing encapsulation of TiO_x overlayer on metallic Ru nanoparticles can be acquired in the following reduction of this oxide interphase. In contrast, the SMSI generation by the conventional mechanism is highly suppressed over the RuO_2/TiO_2 phase calcined at a low temperature. Thanks to this improved SMSI on Ru/TiO_2 catalyst, it thus possesses an excellent performance in CO_2 methanation, with a promoted CO_2 conversion activity. Our findings suggest a different mechanism for the SMSI generation through the oxide interphase formation, and it also offers an alternative pathway to tune catalytic properties of supported metal catalysts.

Introduction

The strong metal–support interaction (SMSI) was first discovered by Tauster et al. to describe the phenomenon that reducible oxides supported group VIII noble metals suffer a significant suppression of CO and H_2 chemisorption after high-temperature reduction treatment.[1, 2, 3, 4] Generally, the pre-existing metal nanoparticles on the supports was suggested during the processes of SMSI, on which the subsequent migration of supports occurs over metal nanoparticles in a reduction condition which is regarded as the classical formation mechanism of SMSI. For decades, researchers have devoted their efforts to exploring the other possible pathways for SMSI formation, in which extensive mechanisms, including the oxidative SMSI,[5, 6, 7] adsorbate-mediated SMSI,[8] reaction-induced SMSI[9, 10] and carbonization-induced SMSI,[11] have been developed so far in terms of the varied formation conditions for the migration of supports over metal nanoparticles.

According to the classical formation mechanism, the SMSI generation was greatly reliable to the preferable reducibility of metal oxide. However, due to the chemical interactions of metal oxide with the supports which is also oxide in many cases, the formation of solid solution of oxide interphase would encounter during the pretreatment of precursors in the practical synthesis of metals on the supports, which makes the stepwise reduction of metal oxides to metallic nanoparticles on support a challenge. In this case, the mechanism of SMSI generation would differ from the classical SMSI. More recently, the researches have also demonstrated that the migration of support components is greatly sensitive to the contact interface between metal and support in an SMSI system,[12, 13] while a mechanistic understanding for the role of reduction mechanism in this state of SMSI formation is still lacking.

Herein we have focused on the effect of virgin catalyst states on SMSI formation in the Ru/TiO_2 catalytic system. Benefiting from the similar crystal parameters between RuO_2 and rutile TiO_2, an epitaxial growth

of RuO_2 on rutile TiO_2 can be observed after calcination treatment on the Ru/TiO_2 catalyst, which results in the formation of a $Ru_xTi_{1-x}O_2$ interphase between RuO_2 and rutile TiO_2. With increasing the pre-calcination temperature of Ru/TiO_2 catalysts, the $Ru_xTi_{1-x}O_2$ interphase with the Ru–O–Ti bonding can be effectively augmented. More importantly, it leads to an enhanced TiO_x overlayer on Ru nanoparticles, through a co-reduction of Ru and Ti in the Ru–O–Ti bonds in the H_2 reduction treatment. It thus demonstrates that the formation of SMSI by the co-reduction mechanism becomes predominant than the classical one in this Ru/TiO_2 catalyst. Considering that the SMSI of metal/support catalysts has played a key role in heterogeneous catalysis which has attracted worldwide interest, especially in CO/CO_2 hydrogenation reactions,[14, 15, 16] for which the catalytic CO_2 methanation is taken as a prototype reaction to probe the SMSI effect of Ru/TiO_2 catalyst. Thanks to this improved SMSI on Ru/TiO_2, it thus possesses an excellent performance in CO_2 methanation, with a promoted CO_2 conversion activity. This work provides an additional formation mechanism of SMSI and offers an opportunity to tailoring the catalytic performance by SMSI.

Results

The Ru/TiO_2 catalysts in this work were obtained with a wet impregnation method by loading the $RuCl_3$ precursor onto a rutile-type TiO_2, followed by calcination in air at different temperatures to acquire a varied chemical interaction between RuO_2 and rutile TiO_2. The resulting samples after calcination and a chlorides removal process are denoted as Ru/TiO_2-*x*Air, where *x* indicates the intended calcination temperature (200, 300, 400, or 500°C). The loading of Ru in the Ru/TiO_2-*x*Air is 2.25 wt% as determined by the inductively coupled plasma optical emission spectroscopy (ICP-OES).

Structure Identification. All the Ru/TiO_2-*x*Air samples possess similar surface areas and pore volumes as indicated by N_2 physisorption (Table S1). The X-ray diffraction (XRD) patterns of the Ru/TiO_2-*x*Air samples do not show any diffraction associated with Ru or RuO_2 species (Figure S1), suggesting the high dispersion of Ru species on the rutile TiO_2 after calcination, which is further confirmed by the highly dispersed Ru/Ti/O in the elemental mapping results (Figure S2).

As rutile TiO_2 and RuO_2 own the same crystal space group with comparable lattice parameters (Table S2), the calcination treatment of Ru/TiO_2 is expected to trigger a chemical solid solution between RuO_2 and rutile TiO_2,[17] which is then investigated by various characterizations. As shown in Fig. 1a, the Raman spectrum of the TiO_2 support shows characteristic bands of the rutile phase at 447 (E_g) and 612 cm^{-1} (A_{1g}).[18, 19, 20] After the incorporation with RuO_2, a new band associated with RuO_2 appeared at ~ 500 cm^{-1}, suggesting the presence of RuO_2 species in the Ru/TiO_2-*x*Air samples. The E_g bands show a red shift of ~ 30 cm^{-1} after the calcination treatments, which indicates the formation of $Ru_xTi_{1-x}O_2$ interphase (Ru–O–Ti bonding) between RuO_2 and rutile TiO_2.[21] With increasing the calcination temperature, the shift of E_g bands from 420 to 414 cm^{-1} can be originated from the increased proportion of $Ru_xTi_{1-x}O_2$ interphase

in the Ru/TiO_2-*x*Air system. According to the high-resolution transmission electron microscopy (HRTEM) observations in Figure S3, distinct morphologies of the supported Ru species are observed. The Ru/TiO_2-200Air sample possesses dominant RuO_2 nanoparticles (NPs) with clear boundaries on TiO_2 support. In contrast, for the Ru/TiO_2-*x*Air (*x* = 300, 400, or 500°C) samples, the supported RuO_2 NPs can hardly be clearly identified, which implies the proceeding epitaxial growth of RuO_2 on the rutile TiO_2 support to form $Ru_xTi_{1-x}O_2$ interphase after high temperature calcination.

The structure evolution of the Ru/TiO_2-*x*Air samples is further explored by the X-ray absorption spectroscopy (XAS). The X-ray absorption near-edge structure (XANES) results indicate that Ru^{4+} species is dominant in all the Ru/TiO_2-*x*Air samples as their edge energies are found to be similar with that of RuO_2 (Figure S4). From the extended X-ray absorption fine structure (EXAFS) and the fitting results in Fig. 1b and Table S3, increasing the calcination temperature leads to a progressive increase in the coordination number (CN) of Ru–O (~ 1.98 Å) and that of Ru–Ru_2 (~ 3.59 Å). While similar CNs of Ru–Ru_1 in the second shell are observed with a low value of 0.3 ~ 0.5 for all the Ru/TiO_2-*x*Air samples. These findings suggest the facile formation of large but flat RuO_2 islands on TiO_2 during the calcination treatment as illustrated in Fig. 1c. In addition, the Ru/TiO_2-*x*Air samples present an extra coordination environment of Ru–O–Ti bonding (~ 3.00 Å), suggesting the formation of $Ru_xTi_{1-x}O_2$ interphase. The Ru/TiO_2-200Air sample possesses a low coordinated Ru–O–Ti with a CN of only 0.2, indicative of the dominant RuO_2 NPs in the Ru/TiO_2-200Air catalyst. With increasing the calcination temperature from 300 to 500°C, the CN associated with Ru–O–Ti slightly increases from 0.7 to 0.9, which demonstrates the enhancement of $Ru_xTi_{1-x}O_2$ interphase as shown in the white boxes of Fig. 1c. This finding is also in good agreement with that of Raman spectra and TEM observations.

SMSI formation. As reported previously,[22, 23, 24] a high-temperature reduction treatment of Ru/TiO_2 leads to the SMSI of TiO_x overlayer encapsulation over the Ru NPs. To investigate the role of $Ru_xTi_{1-x}O_2$ interphase in SMSI mechanism in Ru/TiO_x catalysts, all Ru/TiO_2-*x*Air samples were then reduced with H_2 at 450°C which were referred as Ru/TiO_2-*x*Air-R. As observed by TEM images (Figures S5), the morphologies of the Ru/TiO_2-*x*Air-R catalysts exhibit a slight aggregation of Ru NPs as the pre-calcination temperature increases. However, no diffraction peak related with Ru species appears in XRD patterns of the Ru/TiO_2-*x*Air-R catalysts (Figures S6), which indicates the formation of flat Ru species on TiO_2 surface as illustrated above in Fig. 1c. The variation of Ru chemical states was then determined by XAS experiments. The XANES spectra of the Ru/TiO_2-*x*Air-R catalysts show a shift of Ru *K*-edge to Ru foil as the pre-calcination temperature increases (Fig. 2a), indicative of an increasing reduction degree of Ru NPs which might be caused by the Ru size enlargement. Confirming from the EXAFS of Ru *K*-edge and the corresponding fitting results (Figure S7 and Table S4), the CN of Ru–Ru pair (~ 2.67 Å) from 2.8 to 7.5 shows an increase with improving the pre-calcination temperature in the Ru/TiO_2-*x*Air-R catalysts. The

HRTEM images in Fig. 2b then reveal that Ru NPs tend to be encapsulated by TiO_x overlayer at a pre-calcination temperature higher than 300°C. With increasing the pre-calcination temperature of the Ru/TiO_2-*x*Air-R catalysts, an obvious decrease of CO chemisorption is observed (Figure S8 and Table S5), which in turn indicates the growth of TiO_x overlayer as observed in the HRTEM images.

Diffuse reflectance infrared Fourier transform spectra of CO (CO-DRIFTS) were used to probe the structure evolution of the Ru/TiO_2-*x*Air-R catalysts. As shown in Fig. 2c, there are three distinct models associated with CO adsorption on the Ru NPs over the Ru/TiO_2-*x*Air-R catalysts. The band at 2030 ~ 2050 cm^{-1} is assigned to linear CO adsorption on metallic Ru NPs,[25, 26, 27, 28] while the bands at 2136 and 2075 cm^{-1} are related to CO adsorption on partially oxidized Ru^{n+} species.[27, 29, 30, 31] An enhanced proportion of the metallic Ru was observed with the increase of the pre-calcination temperature, which indicates the improvement of Ru reduction as observed by XAS results. The weakened intensity of CO adsorption together with the red shift of bands related to metallic Ru implied the decreased CO coverage,[32] which in turn demonstrated the growing encapsulation of TiO_x overlayer on Ru NPs with increasing the pre-calcination temperature. Therefore, a high pre-calcination temperature is in favor of the reduction of Ru/TiO_2 and the following formation of SMSI in the Ru/TiO_2-*x*Air-R catalysts. In combination with the structural behaviors of the Ru/TiO_2-*x*Air catalysts, the formation of Ru–O–Ti bonding in the $Ru_xTi_{1-x}O_2$ interphase is bound to play a vital role in the facile formation of SMSI during a reduction treatment at 450°C.

SMSI Formation Mechanism. The reduction behaviors of the Ru/TiO_2-*x*Air samples were then explored with H_2-TPR experiments to give a mechanistic understanding of SMSI generation. As shown in Fig. 3a, the Ru/TiO_2-200Air sample exhibits two main reduction peaks (at 65 and 514°C), which are assigned to the reduction of RuO_2 NPs and the TiO_2 substrate, respectively. In terms of the reduction temperature of 450°C in our sample pretreatment, the Ru/TiO_2-200Air sample suffers predominantly the reduction of RuO_2 to metallic Ru phase, while the reduction of TiO_2 to form TiO_x overlayer can hardly occur. As a result, rare SMSI state is observed over the Ru/TiO_2-200Air-R sample, which indicates that the formation of SMSI in the Ru/TiO_2-200Air-R sample would follow the conventional SMSI mechanism as depicted in Fig. 3b. Namely, metallic Ru NPs can be facilely acquired at a low reduction temperature, while the migration of TiO_x overlayer on Ru surface needs a high-temperature reduction treatment due to the relatively inert TiO_2 substrate.

In contrast, the Ru/TiO_2-*x*Air (*x* = 300, 400 or 500°C) samples mainly show one compound reduction peak at ~ 150°C, and their H_2 consumption is about 1.5 times as the theoretical estimation from RuO_2 reduction (Table S6), which indicates the co-reduction of both RuO_2 and TiO_2 species, primarily due to the presence of $Ru_xTi_{1-x}O_2$ interphase. In these cases, the reduction of TiO_2 species becomes facile, which subsequently facilitates the formation of SMSI states. According to the above observations, we have proposed a co-reduction mechanism for the formation of SMSI in the Ru/TiO_2-*x*Air (*x* = 300, 400 or 500°C) systems as illustrated in Fig. 3c. By the high-temperature calcination treatment of Ru/TiO_2, the RuO_2

proceeds an epitaxial growth on the rutile TiO_2 support to form $Ru_xTi_{1-x}O_2$ interphase. Benefiting from the presence of Ru–O–Ti bonding in the $Ru_xTi_{1-x}O_2$ interphase, the co-reduction of Ru and Ti can be greatly facilitated upon H_2 treatment, which leads to an enhancement of TiO_x overlayer on Ru NPs consequently. Therefore, we can speculate that a low-temperature reduction treatment of the Ru/TiO_2-*x*Air ($x \geq 300$°C) can also lead to SMSI due to facile co-reduction of $Ru_xTi_{1-x}O_2$ interphase.

CO_2 Methanation. The methanation of CO_2, known as the Sabatier reaction, is usually promoted by a moderate SMSI.[33, 34, 35] With increasing the pre-calcination temperature of Ru/TiO_2 from 200 to 500°C, an enhanced SMSI can be acquired for the Ru/TiO_2-*x*Air samples reduced at 300°C (Ru/TiO_2-*x*Air-300R catalysts) as reflected by the gradually decreasing CO chemisorption (Table S7). The SMSI acquired by the co-reduction mechanism then provides an effective approach to tuning the catalytic performance of CO_2 methanation. As shown in Fig. 4a and Table S8, all the Ru/TiO_2-*x*Air-300R catalysts exhibit 100% CH_4 selectivity, with the intrinsic activity (reflected as TOF) soaring with increasing the pre-calcination temperature, which benefits from the growing tendency to SMSI generation. In contrast, the Ru/TiO_2-200Air-300R catalyst exhibits a much lower TOF value for the absence of SMSI.

For the Ru/TiO_2-200Air sample, a high-temperature treatment can also lead to a SMSI state similar with the case of classical migration mechanism for SMSI formation. As shown in Fig. 4b, the activity of CO_2 methanation is greatly improved with increasing the reduction temperature from 300 to 600°C, which suggests that the formation of an appropriate SMSI in the Ru/TiO_2 system can greatly promote the performance of CO_2 methanation.

To give a better comparison, we have also fabricated a Ru/TiO_2-300N sample which was calcined in a N_2 atmosphere instead of air to avoid the generation of $Ru_xTi_{1-x}O_2$ interphase. As expected, the reduction of TiO_2 in the Ru/TiO_2-300N sample required a temperature higher than 400°C as reflected by the H_2-TPR result (Figure S9). With increasing the reduction temperature from 300 to 600°C, an enhanced activity of CO_2 methanation is also observed for the Ru/TiO_2-300N samples (Fig. 4b and entries 7–9 in Table S8), confirming of the promotional effect of SMSI on the performance of CO_2 methanation. The activity of the Ru/TiO_2-500Air-300R catalyst is 1.9 and 5.5 times as that of the Ru/TiO_2-200Air-600R and Ru/TiO_2-300N-600R, respectively. It thus further demonstrates the enhanced formation of SMSI by a co-reduction mechanism of the $Ru_xTi_{1-x}O_2$ interphase than the classical migration mechanism on the Ru/TiO_2 catalysts.

Conclusion

In conclusion, the evolution of Ru/TiO_2 catalyst is intensively studied to address the derivation of strong metal-support interaction by varying the calcination temperature. A high calcination temperature treatment favors the formation of extensive Ru–O–Ti bonding in the $Ru_xTi_{1-x}O_2$ interphase, which promotes the co-reduction of Ru and Ti upon H_2 reduction treatment. The facile reduction of TiO_2 species

further leads to an enhancement of migrated TiO_x overlayer. The SMSI can be more easily acquired by the co-reduction mechanism compared with the classical migration mechanism as reflected by the promoted performance of CO_2 methanation. This work gives a new understanding of the SMSI generation mechanism and provides an effective approach to tailoring catalytic properties by SMSI.

Methods

Synthesis of the Ru/TiO_2-x Air samples. Typically, 1.75 g of the ruthenium (III) chloride was diluted with pure water to 50 mL, followed by adding 2.0 g of rutile TiO_2 to the solution with vigorous stirring. Then, the suspension was dried in a 50°C water bath through evaporation, followed by drying at 110°C. The obtained solid was denoted as Ru/TiO_2-dried, which was following calcination in air at an intended temperature (200, 300, 400 or 500°C) for 3 h. Then, a dilute ammonia solution was used to wash the sample repeatedly in order to remove the residual chlorides. The sample after an overnight drying at 60°C was then denoted as Ru/TiO_2-*x*Air, where *x* indicates the intended calcination temperature (200, 300, 400 or 500°C). The Ru loading in the Ru/TiO_2-*x*Air catalyst is 2.25 wt% as detected by ICP-OES.

Synthesis of the Ru/TiO_2-300N sample. The Ru/TiO_2-300N sample was acquired by calcining the Ru/TiO_2-dried in a nitrogen flow at 300°C, followed by the same chlorides removal treatment as that for acquiring the Ru/TiO_2-*x*Air samples. The Ru loading in the Ru/TiO_2-300N catalyst is 2.32 wt% as detected by ICP-OES.

The Ru/TiO_2 samples reduced with H_2 at a desired temperature (X = 300, 450 or 600) were then denoted as Ru/TiO_2-*x*Air-XR or Ru/TiO_2-300N-XR catalysts. Unless stated, the Ru/TiO_2-*x*Air-450R appears in the form of Ru/TiO_2-*x*Air-R.

Characterization. The Ru loadings were determined by inductively coupled plasma optical emission spectroscopy (ICP-OES) with an ICP-OES 7300DV instrument. Powder X-ray diffraction (XRD) data were recorded using a PANalytical X'Pert-Pro X-ray diffractometer with Cu Kα radiation source (λ = 0.15432 nm). Nitrogen adsorption-desorption isotherm was performed with a Micromeritics ASAP 2460 instrument at − 196°C. High-angle annular dark field scanning transmission electron microscopy (HAADF-STEM), elemental mapping, and high-resolution transmission electron microscopy (HRTEM) images were acquired using a JEOL JEM-2100F microscope operating at 200 kV. Raman spectra were recorded with a dispersive Horiva Jobin Yvon LabRam HR800 microscope equipped with a He-Ne laser (633 nm).

X-ray absorption spectroscopy (XAS) data at the Ru *K*-edge, including extended X-ray absorption fine structure (EXAFS) and X-ray absorption near-edge structure (XANES), were acquired at the BL 14W1 of Shanghai Synchrotron Radiation Facility (SSRF), China. The Ru/TiO_2-*x*Air sample was squashed into a wafer in air and sealed with Capton film, while the Ru/TiO_2-*x*Air-R sample was first pretreated with H_2 at 450°C for 2 h, followed by sealing with Capton film in a glove box. The spectrum was collected in the transmission mode, following which the acquired data were analyzed with the Athena software package.

Diffuse reflectance infrared Fourier transform spectrum (DRIFTS) was recorded on a Bruker Equinox 55 spectrometer. For each CO adsorption, the sample was *in situ* pretreated with H_2 for 1 h at 450°C, followed by cooling down to 25°C. The gas flow was then switched to He and held for 0.5 h, following which the background spectrum was collected. Then, a 5 vol% CO/He was introduced into the system until achieving a saturated adsorption of CO. Subsequently, the system was purged with He to remove gaseous CO, following which the DRIFT spectrum of CO adsorption was collected.

CO chemisorption was employed with a Micromeritics AutoChem II 2920 instrument. The sample was pretreated with H_2 for 1 h at a designed temperature, followed by purging with He for 0.5 h to remove surface adsorbed H species. Then, the sample was cooled down to 50°C, and a 5 vol% CO/He was repeatedly injected into the reactor until acquiring a saturated CO adsorption. CO microcalorimetric measurements were conducted at 40°C using a BT 2.15 Calvet calorimeter which is equipped with MKS 698A Baratron capacitance manometers. The sample was pretreated with H_2 for 1 h at 450°C, followed by evacuation at 460°C for 0.5 h. After cooling down to room temperature, the quartz tube was tightly sealed followed by transferring to the calorimetric cell and outgassing at 40°C overnight. Then, CO microcalorimetry was carried out during the stepwise import of CO at 40°C.

H_2 temperature-programmed reduction (H_2-TPR) was also conducted with a Micromeritics AutoChem II 2920 apparatus. The sample was pretreated with Ar for 1 h at 200°C, followed by cooling down to 50°C. Then, a 10 vol% H_2/Ar was introduced into the system by heating the sample from 50 to 800°C.

CO_2 hydrogenation. CO_2 hydrogenation tests were performed in a fixed-bed quartz reactor with an inner diameter of 10 mm. Typically, 0.1 g of Ru/TiO_2 catalyst was diluted with 1.0 g of quartz sand and then loaded into the reactor. Prior to catalytic testing, the sample was *in situ* reduced with H_2 for 2 h at a designed temperature, followed by cooling down to the reaction temperature. Then, the feed gas ($H_2/CO_2/N_2$ = 70/20/10 (v/v/v)) was introduced into the reactor for CO_2 hydrogenation tests, in which N_2 was used as an internal standard. The tests were carried out at 200°C, 0.1 MPa and 60,000 mL g_{cat}^{-1} h^{-1}. After passing through an ice-bath (0°C), the gaseous components were analyzed online with an A90 Echrom gas chromatograph which was equipped with a TDX-01 column connected to a thermal conductivity detector (TCD).

Declarations

Data availability

The data that support the plots within this study are available from the corresponding author on reasonable request.

Acknowledgments

This work was financially supported by the National Key R&D Program of China (2016YFA0202804), the Strategic Priority Research Program of the Chinese Academy of Sciences (XDB36030200), the National Natural Science Foundation of China (21978286, 21925803, 21776269), and the Youth Innovation Promotion Association CAS. The EXAFS data were acquired at the BL14W1 of Shanghai Synchrotron Radiation Facility (SSRF), China.

Competing interests

The authors declare no competing financial interests.

References

1. Tauster SJ, Fung SC, Baker RTK, Horsley JA. Strong interactions in supported-metal catalysts. *Science* **211**, 1121–1125 (1981).
2. Tauster SJ. Strong metal–support interactions. *Acc Chem Res* **20**, 389–394 (1987).
3. Tauster SJ, Fung SC, Garten RL. Strong metal–support interactions. Group 8 noble metals supported on titanium dioxide. *J Am Chem Soc* **100**, 170–175 (1978).
4. Tauster SJ, Fung SC. Strong metal–support interactions: Occurrence among the binary oxides of groups IIA–VB. *J Catal* **55**, 29–35 (1978).
5. Tang H*, et al.* Oxidative strong metal–support interactions (OMSI) of supported platinum-group metal catalysts. *Chem Sci* **9**, 6679–6684 (2018).
6. Tang H*, et al.* Strong metal–support interactions between gold nanoparticles and nonoxides. *J Am Chem Soc* **138**, 56–59 (2015).
7. Liu X*, et al.* Strong metal–support interactions between gold nanoparticles and ZnO nanorods in CO oxidation. *J Am Chem Soc* **134**, 10251–10258 (2012).
8. Matsubu JC*, et al.* Adsorbate-mediated strong metal–support interactions in oxide-supported Rh catalysts. *Nat Chem* **9**, 120–127 (2016).
9. Dong J*, et al.* Reaction-induced strong metal-support interactions between metals and inert boron nitride nanosheets. *J Am Chem Soc* **142**, 17167–17174 (2020).
10. Li Z*, et al.* Reactive metal–support interactions at moderate temperature in two-dimensional niobium-carbide-supported platinum catalysts. *Nat Catal* **1**, 349–355 (2018).
11. Dong J, Fu Q, Jiang Z, Mei B, Bao X. Carbide-supported Au catalysts for water-gas shift reactions: A new territory for the strong metal–support interaction effect. *J Am Chem Soc* **140**, 13808–13816 (2018).
12. Liu J. Advanced electron microscopy of metal–support interactions in supported metal catalysts. *ChemCatChem* **3**, 934–948 (2011).
13. Du X*, et al.* Size-dependent strong metal-support interaction in TiO_2 supported Au nanocatalysts. *Nat Commun* **11**, 5811–5818 (2020).

14. Hernandez Mejia C, van Deelen TW, de Jong KP. Activity enhancement of cobalt catalysts by tuning metal-support interactions. *Nat Commun* **9**, 4459–4466 (2018).
15. van Deelen TW, Hernández Mejía C, de Jong KP. Control of metal-support interactions in heterogeneous catalysts to enhance activity and selectivity. *Nat Catal* **2**, 955–970 (2019).
16. Li S*, et al.* Tuning the selectivity of catalytic carbon dioxide hydrogenation over iridium/cerium oxide catalysts with a strong metal–support interaction. *Angew Chem Int Ed* **56**, 10761–10765 (2017).
17. Lin Q, Liu XY, Jiang Y, Wang Y, Huang Y, Zhang T. Crystal phase effects on the structure and performance of ruthenium nanoparticles for CO_2 hydrogenation. *Catal Sci Technol* **4**, 2058–2063 (2014).
18. Swamy V. Size-dependent modifications of the first-order Raman spectra of nanostructured rutile TiO_2. *Phys Rev B* **77**, 195414 (2008).
19. Busca G, Ramis G, Amores JMG, Escribano VS, Piaggio P. FT Raman and FTIR studies of titanias and metatitanate powders. *J Chem Soc Faraday Trans* **90**, 3181–3190 (1994).
20. Carballo JMG*, et al.* Insights into the deactivation and reactivation of Ru/TiO_2 during Fischer–Tropsch synthesis. *Catal Today* **214**, 2–11 (2013).
21. Martínez Tejada LM, Muñoz A, Centeno MA, Odriozola JA. In-situ Raman spectroscopy study of Ru/TiO_2 catalyst in the selective methanation of CO. *J Raman Spectrosc* **47**, 189–197 (2016).
22. Komaya T*, et al.* The influence of metal–support interactions on the accurate determination of Ru dispersion for Ru/TiO_2. *J Catal* **149**, 142–148 (1994).
23. Zhang Y*, et al.* Ru/TiO_2 catalysts with size-dependent metal/support interaction for tunable reactivity in Fischer–Tropsch synthesis. *ACS Catal* **10**, 12967–12975 (2020).
24. Zhang Y*, et al.* Tuning reactivity of Fischer–Tropsch synthesis by regulating TiO_x overlayer over Ru/TiO_2 nanocatalysts. *Nat Commun* **11**, 3185–3192 (2020).
25. Robbins JL. Chemistry of supported Ru: CO-induced oxidation of Ru at 310 K. *J Catal* **115**, 120–131 (1989).
26. Solymosi F, Raskó J. An infrared study of the influence of CO adsorption on the topology of supported ruthenium. *J Catal* **115**, 107–119 (1989).
27. Panagiotopoulou P, Verykios XE. Mechanistic study of the selective methanation of CO over Ru/TiO_2 catalysts: Effect of metal crystallite size on the nature of active surface species and reaction pathways. *J Phys Chem C* **121**, 5058-5068 (2017).
28. Abdel-Mageed AM, Widmann D, Olesen SE, Chorkendorff I, Behm RJ. Selective CO methanation on highly active Ru/TiO_2 catalysts: Identifying the physical origin of the observed activation/deactivation and loss in selectivity. *ACS Catal* **8**, 5399–5414 (2018).
29. Hadjiivanov K, Lavalley J-C, Lamotte J, Maugé F, Saint-Just J, Che M. FTIR study of CO interaction with Ru/TiO_2 catalysts. *J Catal* **176**, 415–425 (1998).

30. González-Carballo JM, Pérez-Alonso FJ, García-García FJ, Ojeda M, Fierro JLG, Rojas S. In-situ study of the promotional effect of chlorine on the Fischer–Tropsch synthesis with Ru/Al_2O_3. *J Catal* **332**, 177–186 (2015).
31. Elmasides C, Kondarides DI, Grünert W, Verykios XE. XPS and FTIR Study of Ru/Al_2O_3 and Ru/TiO_2 catalysts: reduction characteristics and interaction with a methane–oxygen mixture. *J Phys Chem B* **103**, 5227–5239 (1999).
32. Pfnür H, Menzel D, Hoffmann FM, Ortega A, Bradshaw AM. High resolution vibrational spectroscopy of CO on Ru(001): The importance of lateral interactions. *Surf Sci* **93**, 431–452 (1980).
33. Li J, *et al.* Enhanced CO_2 methanation activity of Ni/anatase catalyst by tuning strong metal–support interactions. *ACS Catal* **9**, 6342–6348 (2019).
34. Xu J, *et al.* Influence of pretreatment temperature on catalytic performance of rutile TiO_2-supported ruthenium catalyst in CO_2 methanation. *J Catal* **333**, 227–237 (2016).
35. Guo Y, *et al.* Low-temperature CO_2 methanation over CeO_2-supported Ru single atoms, nanoclusters, and nanoparticles competitively tuned by strong metal–support interactions and H-spillover effect. *ACS Catal* **8**, 6203–6215 (2018).

Figures

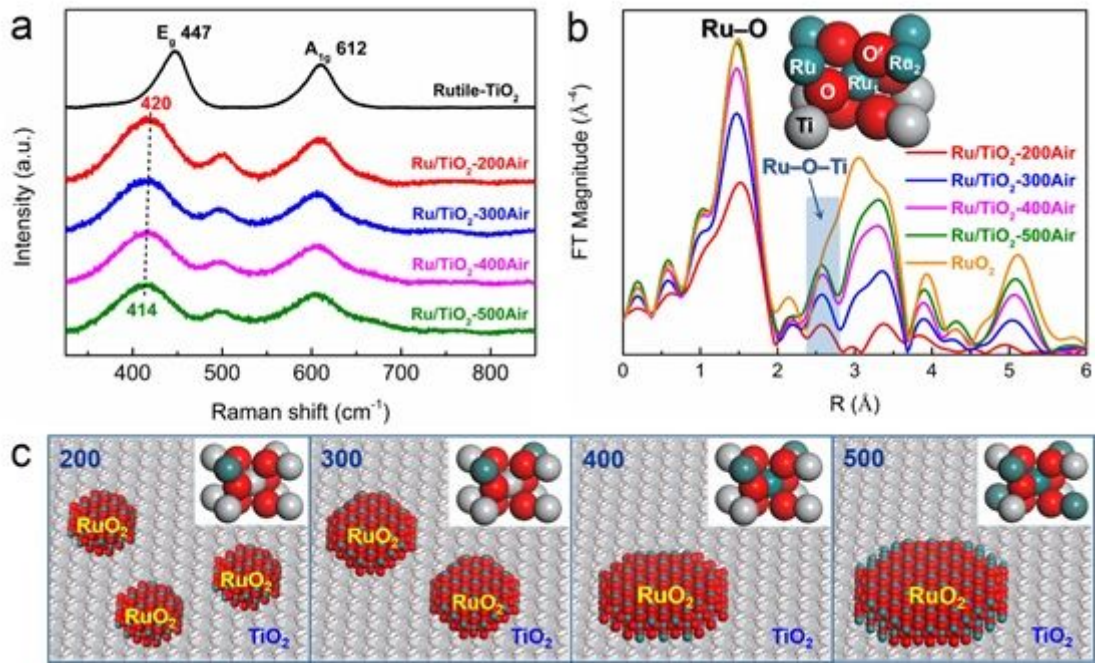

Figure 1

Structure evolution of the Ru/TiO2-xAir catalysts. (a) Raman spectra of rutile TiO2, Ru/TiO2-dried, and the Ru/TiO2-xAir catalysts. (b) Fourier transforms of the k3-weighted EXAFS spectra of Ru K-edge for Ru foil, RuO2, and the Ru/TiO2-xAir catalysts, respectively. (c) A schematic illustration of the structural evolution of Ru/TiO2-xAir catalysts as the calcination temperature varied from 200 to 500 °C.

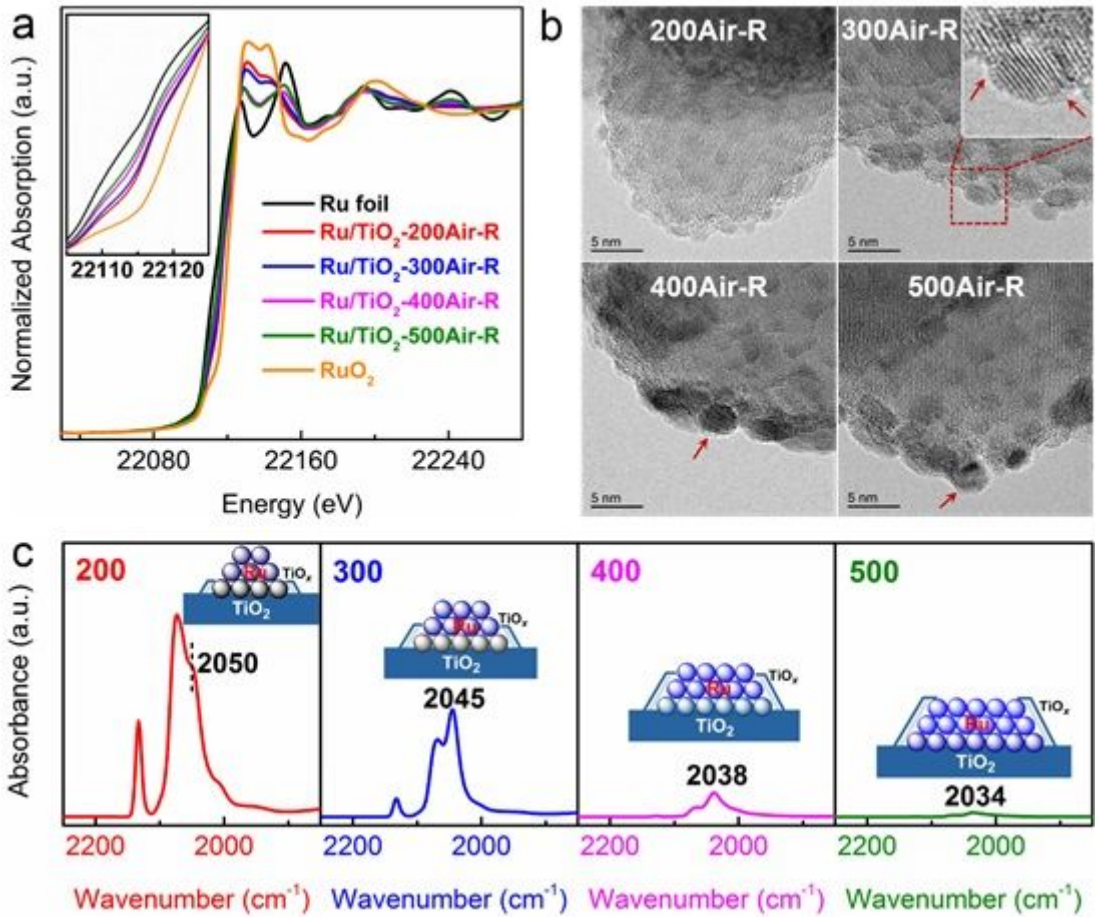

Figure 2

Structure identification of the Ru/TiO2-xAir catalysts after 450 °C reduction (Ru/TiO2-xAir-R samples). (a) Normalized XANES spectra at the Ru K-edge for Ru foil, RuO2, and the Ru/TiO2-xAir-R catalysts. (b) HRTEM images of the Ru/TiO2-xAir-R catalysts. (c) In situ DRIFT spectra obtained after CO adsorption and evacuation with helium at room temperature (25 °C), over the Ru/TiO2-xAir-R catalysts.

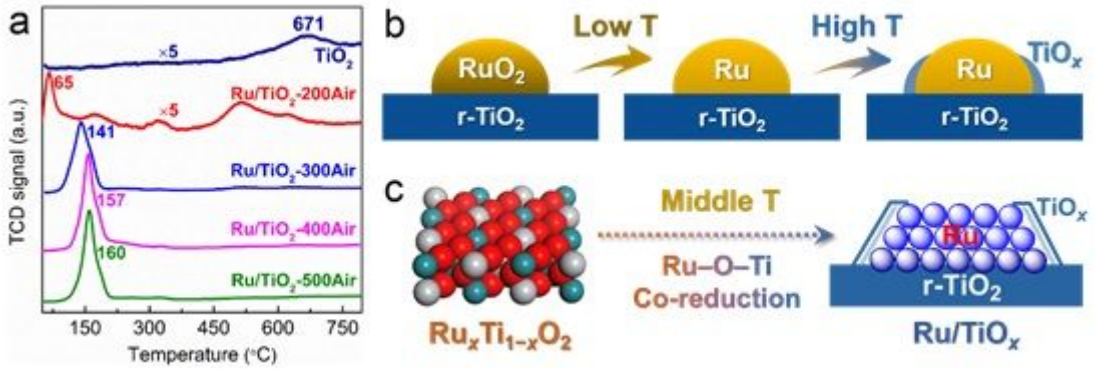

Figure 3

(a) H2-TPR profiles of the Ru/TiO2-xAir catalysts as well as the TiO2 support. (b) A classical support migration mechanism for SMSI formation, as in the case of the Ru/TiO2-200Air sample. (c) A proposed

Ru–O–Ti co-reduction mechanism for facile formation of SMSI, as in the cases of the Ru/TiO2-xAir (x = 300, 400 or 500 °C) samples.

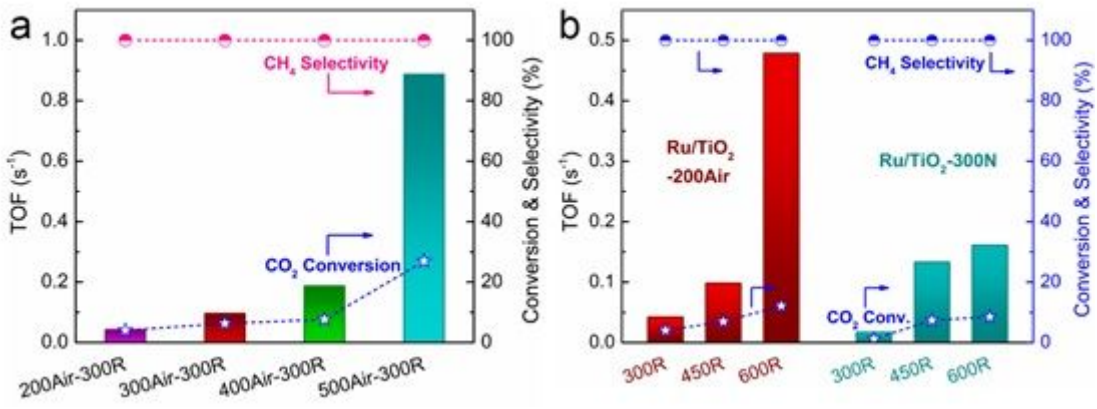

Figure 4

(a) Catalytic performance of the series Ru/TiO2-xAir-300R catalysts for CO2 methanation. (b) Catalytic performance for CO2 methanation over the Ru/TiO2-200Air and Ru/TiO2-300N catalysts pretreated at different temperatures. Reaction conditions: 0.1 MPa, 200 °C, space velocity = 60000 mL h−1 gcat−1, H2/CO2/N2 = 70/20/10.

Supplementary Files

This is a list of supplementary files associated with this preprint. Click to download.

- SupplementaryInformation.docx
- GraphicAbstract.pdf